Fuel 179 (2016) 339–352

Contents lists available at ScienceDirect

Fuel

journal homepage: www.elsevier.com/locate/fuel

N-heptane micro pilot assisted methane combustion in a Rapid Compression Expansion Machine

Stéphanie Schlatter, Bruno Schneider *, Yuri M. Wright, Konstantinos Boulouchos

Aerothermochemistry and Combustion Systems Laboratory, ML Building, ETH Zurich, 8092 Zurich, Switzerland

ARTICLE INFO

Article history:
Received 1 October 2015
Received in revised form 2 March 2016
Accepted 3 March 2016
Available online 29 March 2016

Keywords:
Rapid Compression Expansion Machine
Dual fuel combustion
Pilot ignition
Schlieren

ABSTRACT

The autoignition and combustion behaviour of an n-heptane spray in a premixed methane/air charge was investigated. A Rapid Compression Expansion Machine (RCEM) with a free floating piston was employed to reach engine relevant conditions at Start of Injection (SOI) of the micro n-heptane pilot. The methane content in the ambient gas mixture was varied by injecting different amounts of methane directly into the combustion chamber; the ambient equivalence ratio for the methane content ranged from 0.0 to 0.99. Filtered OH^* chemiluminescence images of the combustion were taken with a UV intensified camera at a rate of 20 kHz through the optical access in the piston and schlieren imaging was performed at 20 kHz for the detection of density gradients arising from pilot injection, ignition and flame propagation in the unburned mixture. Filtered photomultiplier signals of the total emitted light for OH^*, CH^* and C_2^* radicals as well as the pressure signal were simultaneously recorded and the effect of methane content, charge temperature and ambient oxygen concentration on ignition locations, ignition timing and combustion behaviour was analysed. It was found that increasing methane contents in the ambient mixture considerably prolongs the ignition delays of the pilot spray due to inhibiting effects of the premixed methane on the reactions leading to high temperature ignition triggered by n-heptane. Longer ignition delays due to lower ambient temperatures or dilution of the ambient oxidizer cause higher heat release during the combustion of the pilot spray, since more methane/air is entrained and mixed with the pilot spray and oxidized simultaneously. This behaviour is reversed with increasing ignition delays arising from increased methane addition. There, lower heat release rates during pilot combustion were observed due to decreased reactivity in the n-heptane spray area. Comparison of different strategies with respect to the determination of high temperature ignition delay highlighted shortcomings as well as the potential in the usage of spectrally filtered chemiluminescence data, since changes in the spectrum of the emitted chemiluminescence are expected to change over time in the case of pilot ignition due to the transition between combustion modes. An assessment of the methane content influence on the ignition reactions by means of homogeneous, adiabatic Perfectly Stirred Reactor (PSR) simulations with a suitable reaction mechanism is further presented which allows for separation of influences and supports the experimental findings.

1. Introduction

Large stationary gas engines for power generation are increasingly popular due to the widespread availability of natural gas and low fuel price. The potential regarding emission reduction of NO_x and particulate matter by the usage of gaseous fuels represents another benefit as well as the possible increase in engine efficiency due to the high research octane number (130) of methane as the main component of natural gas. The combustion of methane also exhibits lower CO_2 emissions compared to engines fuelled with higher hydrocarbons such as Diesel due to its low C/H

Abbreviations: B, Bore; BDC, Bottom Dead Centre; ϵ, Compression Ratio; EGR, Exhaust Gas Recirculation; HCCI, Homogeneous Charge Compression Ignition; HRR, Heat Release Rate; ID_{OH}, Ignition Delay Schlieren; ID_{schl}, Ignition Delay OH^*; OLP, Optical Light Probe; OP, Operating Point; PMT, Photo-Multiplier Tube; PSR, Perfectly Stirred Reactor; RCEM, Rapid Compression Expansion Machine; RCM, Rapid Compression Machine; *s*, Stroke; SOI, Start of Injection; aSOI, (after) Start of Injection; stdv, Standard Deviation, σ; *T*, Temperature; TDC, Top Dead Centre; TTL, Transistor–Transistor Logic.

* Corresponding author.
E-mail address: schneider@lav.mavt.ethz.ch (B. Schneider).

http://dx.doi.org/10.1016/j.fuel.2016.03.006
0016-2361/

ratio, while potentially engine efficiencies of the same order can be achieved. Simultaneous decrease in engine emission and knock tendency can be achieved by applying lean burn combustion systems [1], while the lower peak temperatures also allow for higher compression ratio or boost pressure level, hence increasing the thermal efficiency compared to operation at stoichiometric conditions [2,3]. Additional measures to decrease in-cylinder temperatures and further increase of cycle efficiency through increased compression ratios include Exhaust Gas Recirculation and Miller valve timing [3–5]. Most of these methods however, lower the reactivity of the in-cylinder mixture and can therefore lead to combustion instabilities, incomplete combustion with high unburned hydrocarbon emissions and misfire due to decreased flame speeds as well as reduced combustion efficiency [6]. To successfully implement a lean burn strategy while achieving low exhaust emissions and high thermal efficiency, ignition systems with sufficient energy deposition are needed to ensure reliable combustion initiation [3]. Pilot ignition or dual fuel combustion represents one of these high ignition energy methods, where the gaseous primary fuel is homogeneously mixed with air and ignited by means of injection of a liquid fuel pilot near Top Dead Centre (TDC). The power output of such a combustion system with pilot ignition is generally controlled by the gaseous primary fuel and the pilot fuel contributes only a small fraction up to 10% [7].

In recent years, experimental investigations concerning pilot ignition for gas engines have focused on engine performance, combustion stability, knock and emissions. A summary and overview of these engine studies, the employed engine systems, pilot and main fuel types is given in [8]. Only limited work is documented on the fundamental processes and some of the mostly unidentified interactions between the fuels and combustion regimes [9–11] in which dual fuel combustion or pilot ignition occurs. The combustion of a Diesel spray in atmospheres containing various gaseous hydrocarbons was investigated by the use of a Rapid Compression Machine (RCM). Analysis of ignition and combustion characteristics of the dual fuel system was performed with combustion chamber pressure analysis and the two colour method for soot detection and temperature determination through the optical access [12,13]. In [14,15], engine experiments were complemented by high speed flame luminosity imaging based on endoscopic techniques, which were limited to the luminous phase of the pilot injection ignition and combustion. The influence of nozzle geometry, methane equivalence ratio, EGR dilution of the premixed charge and ambient temperature on the ignition and combustion behaviour of a Diesel pilot spray was investigated in [16,17] with an optically accessible Rapid Compression Expansion Machine based on chemiluminescence imaging and in-cylinder pressure data.

However, these previous studies focused more on the application side of the gas combustion triggered by pilot injection such as multi-component fuels for the pilot spray (i.e. Diesel), dilution with Exhaust Gas Recirculation (EGR) containing heavier species (CO_2) and therefore changing considerably the heat capacity of the ambient mixture or combining the influences of pressure and temperature changes at the start of pilot injection.

In the present study, various optical techniques as well as pressure based combustion analysis on an optically accessible RCEM of pilot ignition in a lean methane/air mixture with emphasis on separating some of the effects present in engine applications were employed. In order to gain further insight into the fundamental processes and their interactions before, during and after ignition of the pilot spray including the transition to premixed combustion, reactive high-speed schlieren measurements were accompanied by 2D OH^* chemiluminescence imaging and spectrally filtered OH^*, CH^* and C_2^* signals. To overcome the effects of multi-component fuels regarding evaporation, ignition reactions and multi-hole nozzles for the pilot spray, n-heptane was chosen as the pilot fuel and injected by a single hole nozzle injector. The lean ambient mixture consisted of methane and air and the influence of O_2 concentration was investigated by dilution with N_2.

The paper is structured as follows: First, the experimental setup along with test conditions, measurement techniques and processing tools is presented. The results are discussed starting from global quantities such as heat release calculations and photomultiplier signals followed by the analysis of the optical schlieren and OH^* images. In a last step, the experimental discussion is accompanied by selective kinetic simulations focusing on trends observed.

2. Experimental setup

The Rapid Compression Expansion Machine (RCEM) used in this study is a highly flexible, free floating piston generic test rig with excellent optical access through the piston and cylinder head windows. Originally designed for spray combustion experiments, the machine has undergone extensive redesign in recent years and has been successfully applied in experimental investigations of HCCI combustion [18,19] as well as premixed natural gas combustion ignited by Diesel micro pilot injection [16], spark plug and pre-chamber spark plug ignition [17]. The RCEM operates in a single cycle mode (compression and partial expansion) and its free floating piston is driven by pressurized air. The desired compression ratio (and therefore thermodynamic states during compression and expansion) is adjusted by selecting suitable initial conditions in the combustion chamber (loading pressure, wall temperatures and mixture composition) and the according air pressure in the driving volume of the machine. The compressed air at the chosen driving pressure is then acting on the piston rod indirectly through hydraulic oil, which first bypasses a sealing cavity to the back of the rod through a throttle valve and generating a slow piston movement. As soon as the working piston rod bypasses the sealing cavity, the oil can flow freely to the back of the rod which is driving the working piston and the fast compression phase starts. A mass balance piston actuates the working piston by hydraulic coupling and moves in the opposite direction of the working piston to ensure a vibration-free operation during the fast compression phase. A full description of the machine, its working principle and the dilution system can be found in [16,17] and is not repeated here. An overview of the machine specifications are given in Table 1.

Table 1
Specifications of the RCEM.

Bore	B = 84 mm
Stroke	s = 120–250 mm
Compression ratio	ϵ = 5–30
Piston bowl	d_{bowl} = 52 mm, 4 mm depth Optical access d_{window} = 52 mm, Fused silica
Cylinder pressure	p_{max} up to 200 bar
Cylinder head	Flat, highly flexible Optical access d_{window} = 52 mm, Sapphire
Pressure detection	Piezoelectric transducer, 0–250 bar
Heating	Head and liner up to 400 K
Injection system	Flexible, multiple injectors
Ignition system	Flexible (spark plug, pilot injector, pre-chamber)
# of experiments	5 per hour

N-heptane (C_7H_{16}) sprays were injected into the combustion chamber of the RCEM containing various mixtures of methane (CH_4) and oxidizer (various amounts of oxygen (O_2)). Details concerning the CH_4 administration and dilution preparation for the machine can be found in [16,17]. The machine is highly flexible in terms of the thermodynamic conditions which are reachable, since the stroke, compression ratio and initial temperature can be adjusted. Multiple optical accesses allow for different optical techniques to be applied such as high speed imaging of chemiluminescence, schlieren and 1D soot measurements which are all outlined in more detail in the sections below. Simultaneously to the optical data, a PC-based transient measurement system records pressure (from a cooled Kistler 7061B piezoelectric transducer in conjunction with a piezoresistive transducer in the intake for pegging) and piston position signals along with control and synchronization signals such as injection, camera and laser triggers at a frequency of 100 kHz.

2.1. Optical diagnostics

A series of optical setups can be installed on the RCEM and different diagnostics are possible through the optical access in the piston and cylinder head, respectively. In the present work, high-speed 2D OH* chemiluminescence recordings are complemented by reactive schlieren images to gain insight in pilot spray mixing, ignition and combustion processes.

2.1.1. OH* chemiluminescence and photomultipliers

High speed 2D OH* chemiluminescence imaging was performed on the RCEM together with spatially integrated light emission measurements for different wavelengths to obtain information about ignition and combustion characteristics. Spatial distribution of OH* chemiluminescence was recorded with an intensified high speed camera (LaVision HSS6 and image intensifier, 12 bits dynamic range) equipped with a 50 mm UV lens (f/2.0) and a bandpass filter for a wavelength of 306 nm and 12.1 nm FWHM. All images were taken at a rate of 20 kHz with the maximum exposure time of 50 μs and 55% gain in order to maximize the signal to noise ratio. The applied setup resulted in a spatial resolution of 0.237 mm/pixel and is schematically represented in Fig. 1. Spatially integrated light emission is recorded by three Hamamatsu H5784-03 photomultiplier tubes (PMT) at a frequency of 100 kHz equipped with the respective bandpassfilters for OH* (310 nm, FWHM 10 nm), CH* (430 nm, FWHM 11 nm) and C_2^* (510 nm, FWHM 8 nm).

In order to investigate the occurrence of soot and the effect thereof on chemiluminescence, an Optical Light Probe (OLP) was mounted on the cylinderhead window, filtering the integrated incident light for 3 different wavelengths (680 nm, 790 nm, 903 nm, for further details see [20]) at a sampling rate of 100 kHz and allowing for a transient 3 colour pyrometry for which further details can be found in [21,22,20,23,24]. For all investigated operating points no signal at maximum gain in any of the three respective channels (corresponding to the three wavelengths) was detected and soot radiation is therefore considered to be negligible in the presented work.

2.1.2. Schlieren high-speed imaging

To visualize refractive index gradients in transparent media such as density gradients in gases, the schlieren technique represents a well established tool which allows for good temporal and spatial resolution while providing information about temperature and composition of the system [25,26]. Due to the very low turbulence levels in the RCEM, reactive schlieren experiments are possible where, in addition to the pilot spray and ignition event,

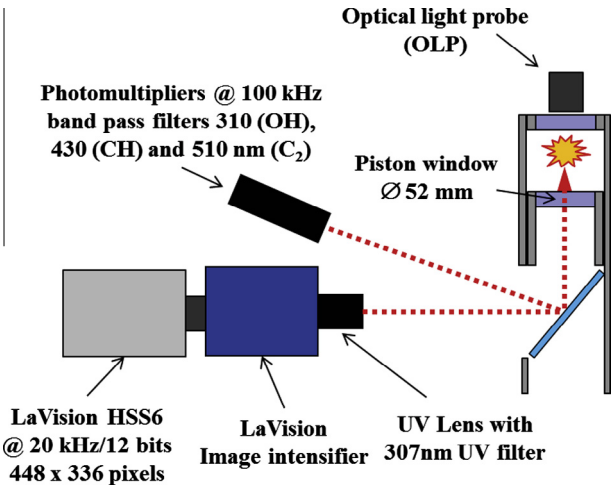

Fig. 1. Schematic of optical arrangement for chemiluminescence and OLP.

the premixed flame front can be visualized. The illumination of the schlieren setup was generated by a pulsed diode laser at a wavelength of 690 nm and a pulse length of 0.05 μs at a frequency of 20 kHz. The light emitted from the laser unit was focused on a 1 mm pinhole and scattered on a diffusion disk, then collimated by the first spherical lens with a focal length of 400 mm and focused again after the cylinder head window with a second spherical lens with a focal length of 400 mm, where a circular schlieren stop of 1 mm diameter was mounted 100 mm away from the recording high speed camera (LaVision HSS6) to generate bright field schlieren signals. The camera was equipped with a 50 mm f/1.2 NIKKOR lens and together with a bandpass filter for the laser wavelength centred at 690 nm with a bandwidth of 10 nm, the optical setup resulted in a resolution of 0.12 mm/pixel. The arrangement of the optical accesses, lenses and recording systems is shown in Fig. 2. The size of the pinhole and schlieren stop were found by trial and error similar as applied in [26,27] for the best results in schlieren signal for both the spray and combustion phase. The laser pulses were delayed by 2.5 μs with respect to the 5 μs long exposure TTL-signals generated by the camera.

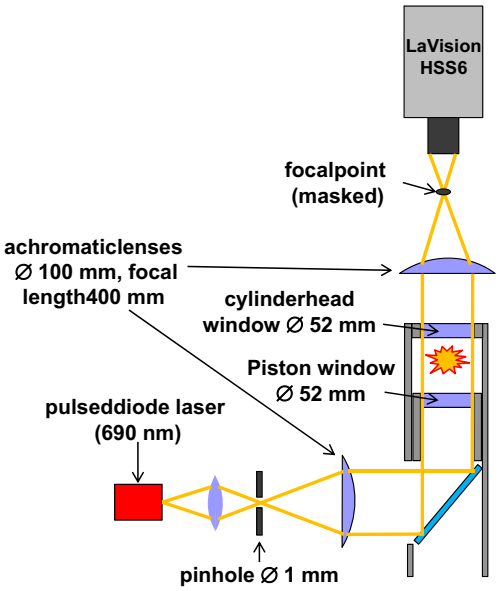

Fig. 2. Schematic of optical arrangement for schlieren.

3. Operating conditions

Three ambient pressure/temperature combinations were assessed with the same pressure evolution (initial and peak pressure) over all operating points and a variation in temperature (and therefore the trapped mass in the combustion chamber). The Start of Injection (SOI) for the n-heptane pilot spray was held constant at a specific pressure level of 17.8 bar with the use of a pressure based triggering system. Fig. 3 shows a sample of the recorded pressure trace and trigger signal, together with the measured piston position of the RCEM. The motion of the free floating piston is determined by the initial piston position as well as the driving pressure and initial chamber pressure. As the piston approaches TDC, it rebounds on the pressure build-up in the chamber due to the compression and any heat release which may arise due to combustion. The RCEM hence approximates the piston motion of a crank case driven piston/connecting rod-assembly only close to TDC, as shown in Fig. 3. Following the SOI trigger signal, however, good agreement between the two kinematics is evident for approximately 8 ms while the duration of interest of the injection/combustion event is about 5 ms, depending on operating condition. The chosen combinations of piston driving and chamber loading pressure correspond to a compression ratio of 12 at an engine speed of 1200 RPM with a crank radius/connecting rod ratio of 0.59. The long stroke of 245 mm was chosen for sufficient clearance height at TDC to avoid strong flow motion from the squish region into the bowl (recessed piston window, cf. Table 1) producing significant turbulence levels potentially obscuring the Schlieren signal.

An overview of the operating points with respect to the temperatures, pressure levels, equivalence ratios, oxygen concentrations and settings of the wall heating is given in Table 2. The pressure based triggering system for the pilot injection leads to a standard deviation of less than 0.6 bar at hydraulic SOI and a temperature standard deviation of maximal 8.6 K (corresponding to 1%), based on the heat release rate analysis of single measurement realizations.

A solenoid common-rail diesel fuel injector equipped with a single hole, 136 µm orifice was used in the experiments which was derived from a standard 7-hole injector by means of welding up six holes. The injection rates, hydraulic injection durations and total injected masses of the micro pilot spray were measured

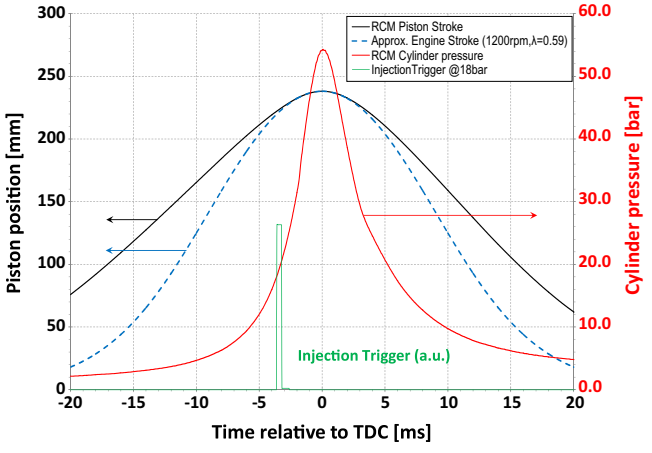

Fig. 3. Cylinder pressure (red) and piston position (black) measured in the RCEM compared to crank driven piston kinematics (blue, dashed) for identical compression ratio and stroke; engine speed corresponds to 1200 RPM. Following the SOI injection trigger signal (green), piston motions agree well for approx. 8 ms. (For interpretation of the references to colour in this figure legend, the reader is referred to the web version of this article.)

Table 2
Operating points and settings of the wall heating.

	OP1	OP2	OP3
T [K] at TDC p [bar] at TDC	980	1027 50.0	1085
T [K] at SOI stdv σ [K]	732 7.8	776 7.2	823 8.6
p [bar] at SOI stdv σ [bar]		17.8 σ = 0.59	
T_{wall} [K]	363	383	403
Φ_{CH_4} O_2 [%]	0–0.66 21	0–0.99 16.8–21	0–0.6 21

with a Bosch tube over 500 injections with a constant rail pressure of 400 bar. The measured injection durations, injected fuel mass in conjunction with the respective standard deviations are given in Table 3.

The geometrical arrangement for both injectors, the optical accesses and the pilot spray is illustrated in Fig. 4. The single hole pilot injector is located 35.26 mm off-axis in the cylinder head with an injection angle of 13.5°. The pilot spray originates 9.26 mm outside of the window, and the injector body creates an additional blind distance of 3.86 mm inside the cylinder head window. The observable domain by schlieren imaging of the pilot spray is therefore starting at 13.12 mm and for the OH^* chemiluminescence (observed through the piston window) 9.26 mm after the nozzle exit. No compensation was applied to the line of sight measurement data due to the injection angle, since the difference in distance along the spray axis over the observable domain is 1.74 mm at most.

3.1. Post-processing

For each investigated operating point two sets of at least 10 experiments each (chemiluminescence and schlieren) were acquired and all data was averaged over all experiments in the respective set. For comparison reasons of the presented experiments, a new fix point had to be set. The fix point for the time base was selected to be the start of injection for the pilot spray including the hydraulic injection delay which is known from the injection rate measurements; the hydraulic delay amounts to approx. 270 µs, cf. Table 3. All signals were shifted during post-processing of the data and the time scale was set to be 0.0 ms at the hydraulic SOI of the pilot spray.

4. Results and discussion

Previous research on methane combustion with pilot ignition in a RCEM has shown several trends with respect to ignition delays and flame spread as a function of pilot injection parameters, methane equivalence ratio and pressure/temperature state of the

Table 3
Micro pilot injections, mass flow rate analysis.

	400 µs	300 µs
Inj. start [µs] stdv σ	270 17	267 11
Inj. end [µs] stdv σ	971 48	825 15
Inj. duration [µs] stdv σ	701 53	558 21
Inj. quantity [mg] stdv σ	1.36 0.06	0.83 0.04

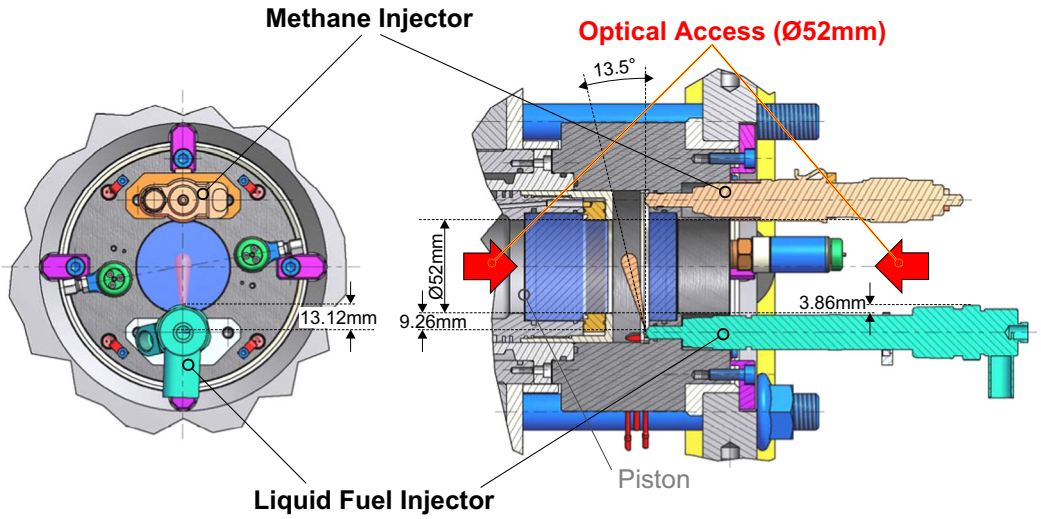

Fig. 4. Top view (left) and section (right) through combustion chamber at TDC illustrating injector configuration and optical access via piston/cylinder head windows.

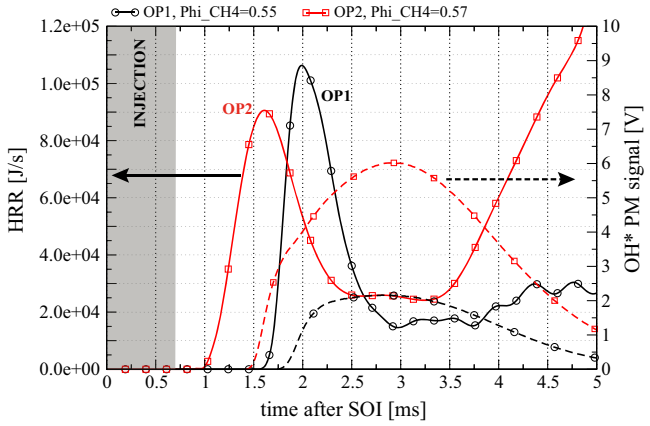

Fig. 5. Influence of temperature (OP1, black vs. OP2, red) on HRR (solid, left *y*-axis) and OH* photomultiplier signals (dashed, right *y*-axis), shaded area shows the measured hydraulic duration of the pilot injection. (For interpretation of the references to colour in this figure legend, the reader is referred to the web version of this article.)

cylinder load, which are reported in [16,17]. The findings from these previous studies were used for the design of the presented work and selection of suitable operating conditions, accompanied by schlieren images providing spray and additional ignition and combustion data plus heat release rate calculations. Temporal evolutions of heat release rates and photomultiplier signals are presented to assess the effects of temperature, pilot mass, methane equivalence ratio and oxygen content on the respective quantities. Data extracted from 2D imaging techniques, namely schlieren and OH* chemiluminescence images, are used to obtain information about pilot spray vapour penetration length, ignition and combustion behaviour under the above listed operating conditions.

4.1. Heat release and chemiluminescence

The data from the heat release rate calculation shows two distinct combustion phases for all investigated operating points (see Fig. 5). The first peak represents the ignition and combustion of the pilot spray with the entrained methane/air. The second phase is the heat released by the premixed flame propagation in the methane/air mixture originating from the ignition spots in the pilot spray. This separation in combustion phases is not observed in the photomultiplier traces (OH* shown) due to the fact that the reactive zones change size over time (from ignition spots to flame propagation) and chemiluminescence emission is a function of temperature which is changing in the system due to compression and expansion. The influence of temperature is shown in Fig. 5: lowering the temperature increases the ignition delay significantly as expected and a higher peak and shorter duration of the heat release during the pilot spray combustion phase can be observed. For the micro pilots studied here, ignition occurs well after the end of injection in both cases, therefore scalar dissipation is unlikely to play a dominant role since it decays rapidly after injection. The prolonged ignition duration however allows for increased spray penetration during which more methane/air is entrained resulting in an larger volume of n-heptane/methane/air mixture. More time is available also for evaporation of the n-heptane droplets and subsequent mixing, therefore stratification and equivalence ratio of n-heptane is expected to be lower for OP1. Since ignition occurs before TDC also for OP1, the temperature difference present at SOI diminishes due to the ongoing compression for the longer ignition delay and the cylinder averaged temperatures at start of ignition (extracted from the heat release analysis) amount to 856 K and 860 K for OP1 and OP2, respectively. Narrower and higher peak heat release rates for longer ignition delays have also been reported for Diesel spray combustion before in [28], where TDC temperatures were lowered systematically while maintaining an identical injection configuration. The changes in HRR were attributed to a more "premixed" conversion of the Diesel fuel due to decreased stratification and these experimental findings are supported by the numerical study of Farrace et al. [29]. In the present investigation, heat release calculations for n-heptane combustion in 'pure' air (i.e. in the absence of methane, equivalence ratio, $\Phi_{CH_4} = 0.0$) could not be performed reliably, since the amount of energy released by the pilot fuel (36 J and 57 J, respectively) is too small compared to uncertainties in the calculation arising from wall heat and mass losses in the system and pressure signal smoothing techniques. Recent Direct Numerical Simulations of a dual-fuel configuration at conditions similar to the ones in the RCEM shortly after SOI, namely 1050 K at 24 bar [30], provide detailed insight concerning the effect of the n-heptane equivalence ratio on heat release rate for a fixed equivalence ratio of the methane/air base charge ($\Phi_{CH_4} = 0.6$), allowing for distinction between the contributions originating from n-heptane and methane conversion. However, as the

droplets – treated in a Lagrangian fashion – are distributed in distinct regions and their initial velocity is set equal to that of the carrier phase (isotropic decaying turbulence with no mean flow), spray dynamics due to fuel injection with large relative droplet velocities are not accounted for and the spatially evolving spray plume structure and entrainment effects during the ignition delay period are not considered. As a consequence, it is difficult to provide estimates on the relative contribution of the entrained methane to the higher pilot spray combustion heat release peak in the present configuration. Finally, heat release rates during the flame propagation phase are observed to increase going from OP1 to OP2 due to higher flame speeds in the ambient methane/air mixture caused by increased reactivity due to the higher temperature. The latter is reflected by the OH* PMT signals showing the expected trend of increased chemiluminescence emissions for OP2 vs. OP1.

The influence of methane equivalence ratio and pilot mass is shown jointly in Fig. 6. With increasing injection duration ignition delays tend to be shorter and more heat is released during the pilot spray combustion phase because of higher fuel mass. The increasing amount of methane has little effect on the ignition delays for the short injection durations as is evident in both the OH* PMT signals and the heat release rate of $OP2_{300}$. Following ignition, comparable heat release rates during the pilot spray combustion phase can be observed for both equivalence ratios for the smaller pilot masses. For the standard injection duration, the higher methane equivalence ratio ($\Phi_{CH_4} = 0.44$ vs. $\Phi_{CH_4} = 0.65$) leads to longer ignition delays. Opposite to what was observed when lowering the temperature, here the longer ignition delay due the higher methane contents results in a decreased heat release peak and an increased duration of the pilot spray combustion phase. This is reflected in the early stages of the OH* emissions, where the higher methane content shows a slower rise between the onset of signal and the time when transition from pilot spray combustion to premixed flame propagation occurs (around 1.6 ms for $\Phi_{CH_4} = 0.44$ and 1.9 ms for $\Phi_{CH_4} = 0.65$); also apparent in the heat release rates. Conversely, during the premixed flame propagation phase, increased OH* intensities and heat release rates can be observed with higher methane content (Fig. 6, bottom), suggesting a strong influence of the premixed flame propagation phase on the OH* emission as discussed later on. More pilot energy manifests itself in a considerable increase in heat release and OH* PMT signals also during the premixed flame propagation phase which is attributed to the larger flame area initialized by the igniting pilot spray. Due to the change in reaction zone area, the variation thereof depending on pilot mass and ignition delay, these observations and conclusions should however be applied cautiously.

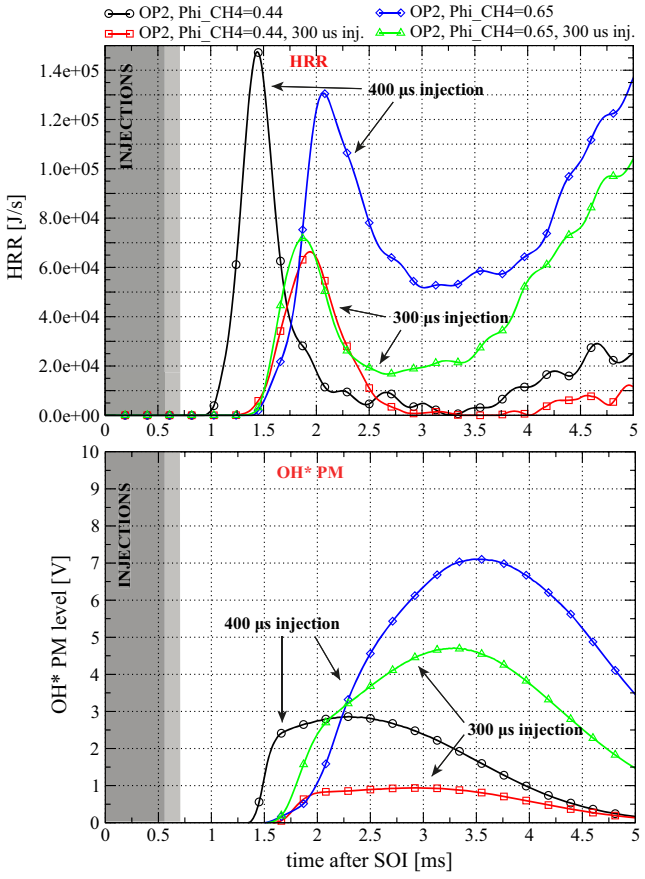

Fig. 6. HRR (top) and OH* photomultiplier signals (bottom) for a variation in pilot mass (OP2 vs. $OP2_{300}$) and equivalence ratios ($\Phi_{CH_4} = 0.44$ vs. $\Phi_{CH_4} = 0.65$). The shaded areas represent the measured hydraulic injection durations of the pilot spray.

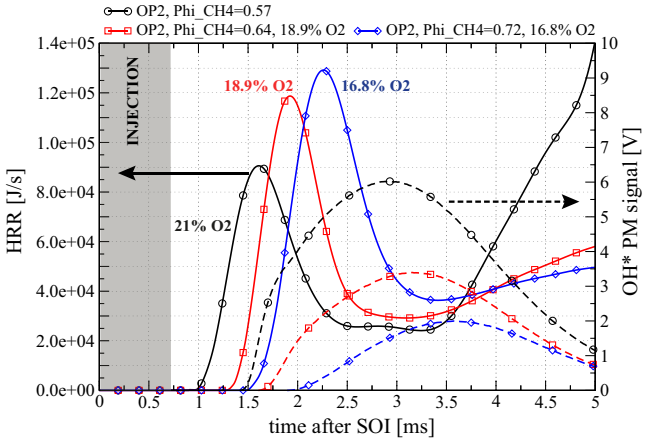

Fig. 7. HRR (solid) and OH* photomultiplier signals (dashed) for OP2 with equal methane masses and different O_2 concentrations (dilution), shaded area represents the measured hydraulic injection duration of the pilot spray.

The influence of oxygen concentration can be seen in Fig. 7. The amount of energy (i.e. methane and pilot mass) is equal in all cases. Due to the difference in ambient oxygen concentration, the methane equivalence ratios differ while the heat capacity of the mixture remains unchanged due to the dilution with N_2. Reduced oxygen concentrations increase the ignition delay and the heat released during the first phase as observed similarly for Diesel spray combustion in the experimental study of [31]. It was seen there, that moderate EGR levels lead to increased heat releases during the premixed part of the spray combustion which has been successfully reproduced also numerically [32]. As discussed above in the context of the temperature sweep, this effect may be intensified with dual fuel combustion, since more methane is entrained in the pilot spray before ignition occurs which is simultaneously oxidized with the pilot fuel, although the present setup does not allow for separation of the respective contributions. With increasing dilution the premixed flame propagation is slowed down considerably due to the substantially reduced reactivity of the mixture and the OH* PMT signals follow the order of the heat release evolutions during this phase, proving strong indication for the dominant effect of the premixed combustion's intensity on OH* emission.

Due to the flat piston geometry and the slow inlet procedure, the turbulence levels in the combustion chamber are very low and cause slow flame propagation during the premixed combustion phase even for equivalence ratios within the flammability limit of methane/air mixtures. Therefore, the fuel conversion in all operating points is seen to be below 100% (a maximum of 80%

was reached) in the thermodynamic analysis of the in-cylinder pressure data.

4.2. Flame spread

The flame area evolution during the combustion can be assessed by the analysis of the respective 2D OH* chemiluminescence images. First, binary images are obtained by applying a threshold of 0.5% of the dynamic range of the camera, corresponding to the maximum intensity detected in the images before ignition occurs. These binary images are temporally integrated, keeping the values in the flame area equal to 1 and normalized by the number of pixels in the window area to know how much of the visible area has ever seen a flame. Fig. 8 shows the evolution of the flame spread in the visible area for OP2 and a sweep in methane content to show the influence of the methane equivalence ratio (Φ_{CH_4} ranging from 0 to 0.65) on the premixed flame propagation. For an equivalence ratio of 0.0, where no methane is present, the reaction zone originating from the n-heptane spray covers about 40% of the window area. With increasing methane content the covered flame area increases for two reasons. First, increasing ignition delays lead to the n-heptane fuel being distributed in a bigger volume (i.e. area in the applied line-of-sight measurement techniques) and subsequently a broader flame area. Second, with an increase in ambient methane equivalence ratio, flame propagation can be sustained at some point and the flame area is increasing over time after the initial flame area generated by the pilot spray. The transition from flame area due to pilot spray combustion to premixed flame propagation is marked as a decrease in the slope of flame spread. For $\Phi_{CH_4} = 0.32$ only minimal flame propagation is observed after 1.4 ms, while the flame propagation starting roughly at 1.9 ms is much faster and spreads through almost the entire window area for an equivalence ratio of $\Phi_{CH_4} = 0.65$. No complete coverage of burnt area in the window area is observed for the shown operating conditions, since the OH* chemiluminescence intensity decreases rapidly with an increase in flame area and the decreasing temperatures in the combustion chamber after TDC is reached (at about 3.5 ms after SOI).

4.3. Intensity distributions

Schlieren imaging in high pressure and high temperature environments is characterized by background structures caused by changes in refractive indices of the ambient gases (temperature/density inhomogeneities) which need to be taken into account when extracting data from schlieren images. Post-processing of the schlieren images was performed by subtracting the background determined in the previous image from the current one, similar to the techniques applied in [33]. The background image ($I_{BG,i-1}$) was obtained by binarising the previous image into signal and no signal, inverting and multiplying it with the previous image to construct an adaptive background image. The processed images were then analysed by a user coded MATLAB routine, which performed an integration of the intensities perpendicular to the spray axis schematically represented in Fig. 9. The obtained intensity distributions for each image were then used to calculate the temporal evolution of the pilot spray penetration and ignition length and to generate 2D maps of the intensities over time. Identical post-processing methods were applied to the OH* chemiluminescence images, except for the background subtraction technique which is not necessary due to the very low signal to noise ratio and the absence of background structures.

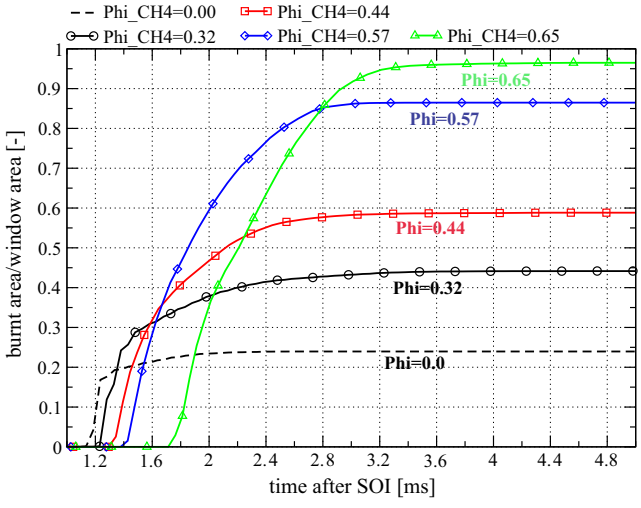

Fig. 8. Evolution of flame area for different methane equivalence ratios calculated by OH* chemiluminescence images, OP2.

The intensity distributions, gained from the post-processed schlieren images provide time-resolved information about spray penetration, ignition location, ignition delay and premixed flame propagation. Fig. 10 shows exemplarily the intensity distribution for OP2 with a methane equivalence ratio $\Phi_{CH_4} = 0.44$ extracted from the schlieren (top) and OH* chemiluminescence images (bottom). Two phases in the time resolved schlieren intensity distribution are visible. The first phase represents the spray entering the observable domain and mixing with the surrounding air/methane mixture. The ignition of the pilot spray and subsequent premixed flame propagation are visible in the second phase which is also found in the OH* intensity distribution. During the second phase, a similar behaviour to the heat release rate is detected with high schlieren intensity peaks right after ignition followed by lower intensities during the premixed combustion phase. The OH* intensity decreases after a certain time during the combustion due to the flame leaving the observable domain, decreasing temperatures and pressures (expansion phase of the piston), while the schlieren distribution is showing intensity due to still remaining density gradients.

The gas phase penetration length of the pilot spray can be extracted from the schlieren intensity distribution by tracking the outer edge of the intensity during the spray phase in every recorded image. The location of the spray tip is found by the location where the schlieren signal reaches a threshold after the maximum detected intensity in the respective picture. The threshold for spray penetration detection was set to 10% of the maximum intensity during the spray phase. The sensitivity of the penetration length dependent on the threshold was assessed for single realizations, where it was found that a threshold of 2% and 5% would lead to the detection of the outer edge of the window or a random spot in the residual background as the spray edge. Setting the threshold to more than 10% leads to earlier disappearance of the spray and shorter penetration lengths.

Fig. 11 shows the measured spread in vapour phase penetration lengths (dashed lines represent minimum and maximum values) over all realizations for two different operating points together with the respective penetration length derived from the averaged data sets (solid lines). The difference between minimum and maximum in penetration length is increasing with time after hydraulic start of injection due to summing up of the deviation over time [34,35]. The spray penetration tends to be higher for OP3 than OP1 due to the lower ambient gas density of 7.50 kg/m^3 for OP3 versus 8.25 kg/m^3 for OP1 at hydraulic start of injection. Also, the penetration length of OP3 is decreasing right before the disappearance of the schlieren signal, indicating that the weakening of the

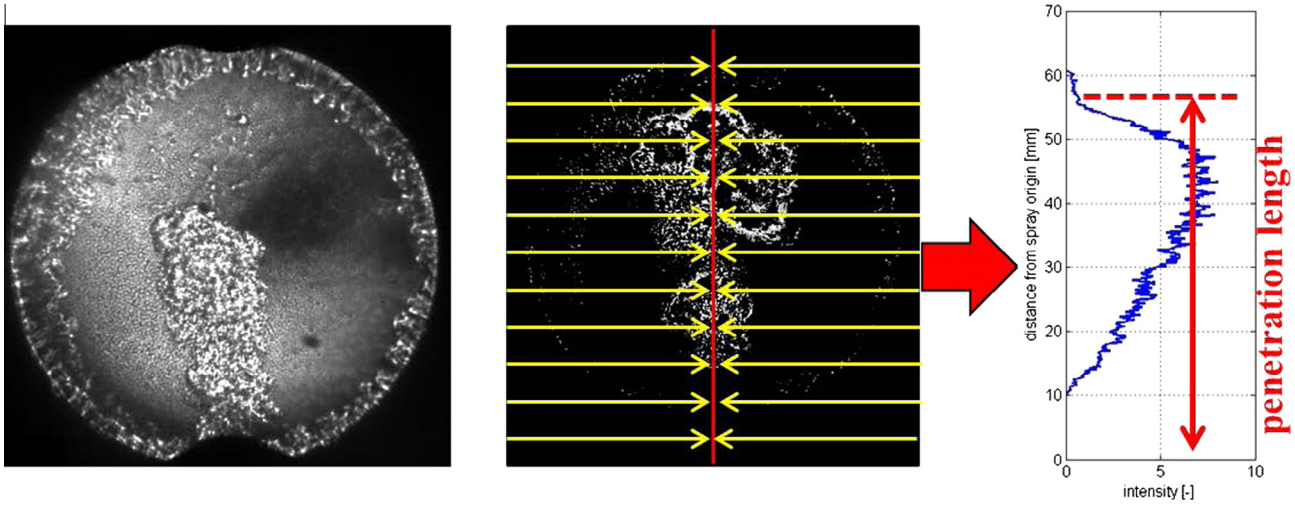

Fig. 9. Unprocessed schlieren image (left), schematic integration of intensity distribution from processed schlieren image (middle) and determination of spray tip penetration from intensity distribution (right).

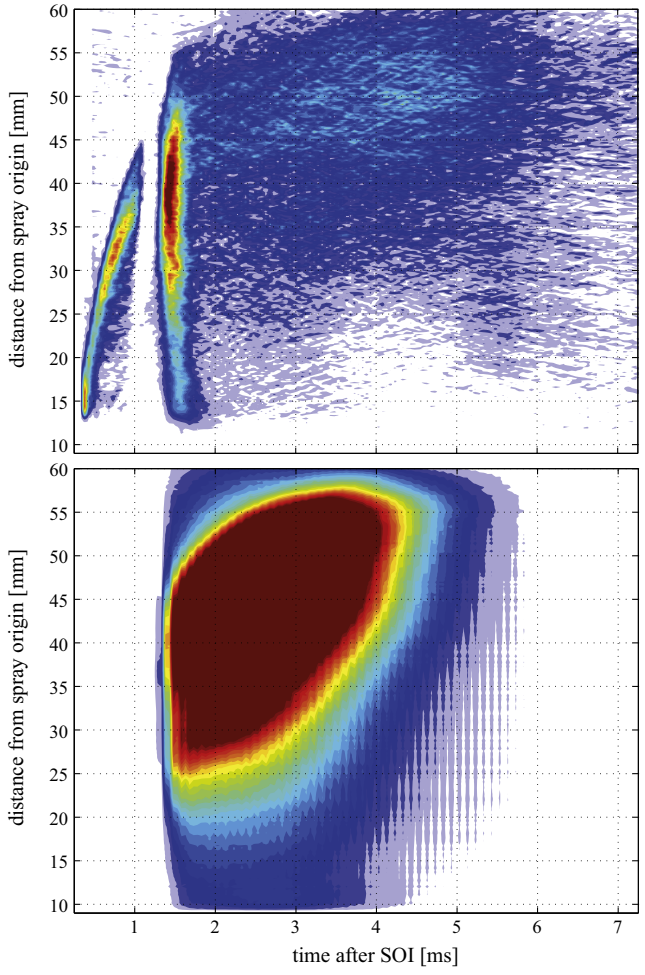

Fig. 10. Intensity distributions for OP2 and Φ_{CH_4} = 0.44 based on schlieren images (top) and OH* chemiluminescence images (bottom).

refractive indices and subsequent disappearance of the spray is starting at the spray tip for this operating point, whereas this effect seems to happen simultaneously in the whole visible spray area in OP1. The weakening of the schlieren signal at the spray tip and the subsequent reduction in vapour phase penetration length has been

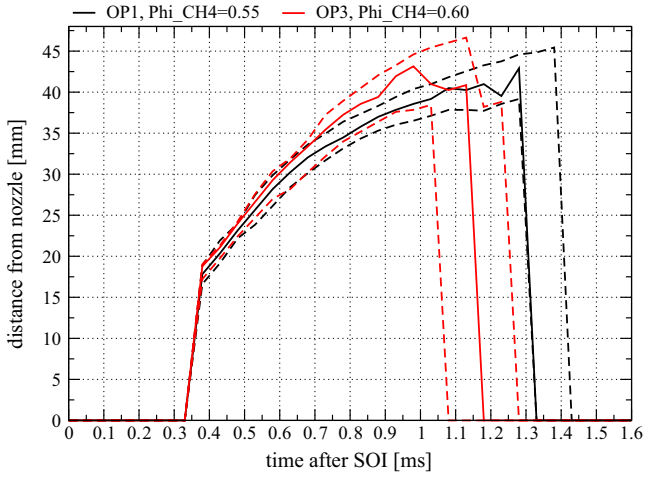

Fig. 11. Mean penetration lengths (solid lines), dashed lines depict the respective minimum and maximum penetration lengths for OP1 (Φ_{CH_4} = 0.55) and OP3 (Φ_{CH_4} = 0.60).

observed before in diesel spray investigations [26] and will be discussed below.

The vapour phase penetration lengths for a sweep in temperature at SOI of the pilot spray (Φ_{CH_4} = 0.43–0.46) are shown in Fig. 12. After the spray enters the visible area just before 0.4 ms after hydraulic SOI, all penetration lengths start at the same value. Due to the difference in ambient densities (ρ_{OP1} = 8.25 kg/m^3, ρ_{OP2} = 8.08 kg/m^3, ρ_{OP3} = 7.31 kg/m^3) at SOI the early penetration lengths of OP2 and OP3 are slightly higher than the one of OP1. While the penetration evolution of OP3 stays the highest until the disappearance of the spray, a flattening effect in the other two traces can be observed before disappearance. The last peak before the disappearance in OP1 and OP2 can be attributed to the weakening of the schlieren signal and a high sensitivity with regards to the applied threshold for penetration detection.

4.4. Ignition delays

Between the two phases in the schlieren intensity distribution, a disappearance or weakening of the schlieren generated by the pilot spray is visible. This was found to happen in all investigated

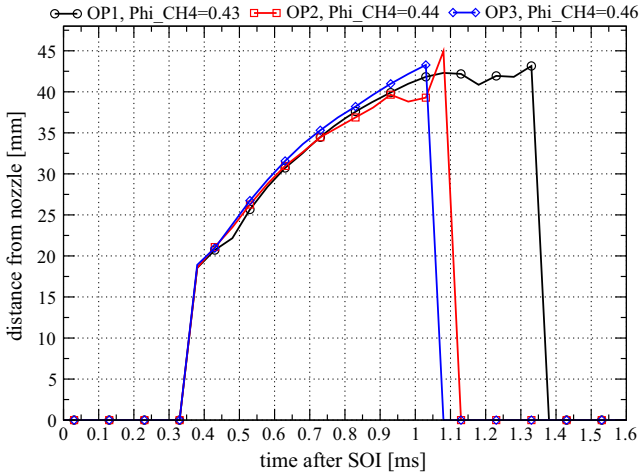

Fig. 12. Penetration lengths (Φ_{CH_4} = 0.43–0.46) extracted from average schlieren intensity distributions for three different temperatures (OP1–OP3).

cases. This phenomena has been observed in spray flames before [26,36,33] and was attributed to low temperature ignition at the spray tip. Based on heat release calculations (small heat release during low temperature ignition), OH* or broadband chemiluminescence and schlieren imaging it was assumed that the small temperature rise during first stage ignition causes the refractive indices in these areas to be very close to the ones in the ambient and therefore cause a transparency phenomena, while OH* chemiluminescence which can be attributed to second stage ignition appeared later in exactly these zones. Only recently this theory could be proven by simultaneous visualization of formaldehyde and schlieren in a spray flame [27]. It was found that in the regions where the softening of the schlieren effect takes place, formaldehyde is produced by the low temperature ignition which is then later consumed by the high temperature ignition and simultaneous reappearance of the refractive index variations.

Fig. 13 shows a time series of averaged schlieren (left half) and OH* chemiluminescence images (right half) for OP2 and Φ_{CH_4} = 0.44 starting at 0.43 ms after hydraulic start of pilot injection. The softening of the schlieren effect is clearly visible (starting at 1.13 ms after SOI) and happens in the entire pilot spray region due to very short injection durations as opposed to localized areas in the spray flames investigated before. The reappearance of the schlieren effect coincides with the onset of OH* chemiluminescence in the same region at 1.43 ms after SOI. Following high temperature ignition the pilot fuel vapour and the entrained methane in the spray plume are consumed rapidly by a propagating ignition front [27,37] and subsequently transition to a deflagrative mode takes place with a slower premixed flame front propagation outwards into the methane/air mixture [37].

Generally, the ignition delay is considered to be the onset of high temperature ignition. In the presented experiments, several ways to calculate the ignition delays are possible, i.e. based on heat release rate calculations, schlieren images, OH* chemiluminescence images and filtered chemiluminescence intensities recorded by the photomultiplier tubes. A determination of ignition delays based on heat release rates is not considered to be suitable for the applied very small pilot masses, since the necessary filtering of piston position traces and pressure data plus mass and heat losses can introduce uncertainties in the order of the heat released by the micro pilot spray and affect greatly the calculation of the ignition timing for the operating points with an ambient equivalence ratio Φ_{CH_4} = 0.0. Therefore, the ignition delays determined by OH* chemiluminescence and schlieren images are compared. Calculation of the ignition delays based on OH* chemiluminescence images is possible and is usually performed when available, but due to the low OH* intensities the maximum exposure time of the camera operating at 20 kHz had to be used and each OH* chemiluminescence image represents a signal integration over 50 μs. In the schlieren setup the laser pulse lasts 0.05 μs and each schlieren image can be seen as a time instant rather than an integrated image (over the course of 50 μs) as in the case of OH* chemiluminescence. Thus, the PMT data is used to determine the ignition delay making use of the five times higher sampling frequency (100 kHz) compared to the 2D OH* system. Ignition from the OH* PMT is set at a threshold of 10% of the maximum value, as applied in previous studies [16,17]. The calculation of the second stage ignition timing from schlieren images was performed in analogy to the procedures in [33] as follows: the intensities in the post-processed schlieren images were spatially integrated to obtain the intensity evolution in time for the observable domain. The time derivative of the intensity evolution then shows a maximum at the second stage ignition due to the fast volumetric ignition phenomena (the subsequent premixed combustion shows lower values due to slow flame propagation).

Fig. 14 presents a comparison of the two methods of ignition delay calculations in a regression plot for OP1 and OP2 (16.8% O_2) and each with a sweep in methane equivalence ratio Φ_{CH_4} together with exponential trendlines for improved visibility. Both ignition delay determination methods show longer ignition delays with increasing amounts of methane in the ambient mixture. The ignition delays calculated by schlieren images ID_{schl} tend to be shorter than the ones calculated by the OH* PMT data ID_{OH} with increasing methane contents, while in [33] they were observed to be the same. Here, this only holds true for the cases with no methane in the ambient mixture (Φ_{CH_4} = 0), where the ID_{OH} are even smaller than ID_{schl}. If the ignition delay increases due to an increase in ambient methane, the difference between the two detection methods increases and the ignition delay based on schlieren imaging ID_{schl} corresponds generally well to the one computed with thermodynamic analysis for the cases with methane in the ambient mixture. Hence, when methane is present in the ambient mixture, a rapid change in refractive indices can be detected before OH* emission is measured. The timing of the high temperature ignition assessed by schlieren analysis with respect to heat release proves that the schlieren effects are in fact caused by density gradients due to heat release while the OH* and CH* emissions are delayed which is shown in Fig. 15 for OP2 (16.8% O_2 and Φ_{CH_4} = 0.99) with the solid blue[1] line representing ID_{schl} and the dashed blue line ID_{OH}, respectively.

One might argue that this behaviour is dependent on the change in O_2 concentration due to the amount of premixed methane which would change the composition and reactivity of the mixture substantially. Fig. 16 shows the same regression plot for OP2 and a sweep in O_2 content in the ambient mixture for two constant methane masses (red and blue) and temperature/pressure conditions leading to prolonged ignition delays due to the lower reactivity. Here, a linear increase in the difference of the two ignition delay calculations is observed represented by the respective trendlines shown in Fig. 16. This provides strong evidence that the methane has a chemical influence (on top of the oxygen concentration) on the ignition processes and lowering chemiluminescence emission during second stage ignition where density gradients due to heat release are detected.

A time delay in chemiluminescence emission and heat release calculation has been observed dominantly in HCCI combustion

[1] For interpretation of colour in Figs. 15 and 16, the reader is referred to the web version of this article.

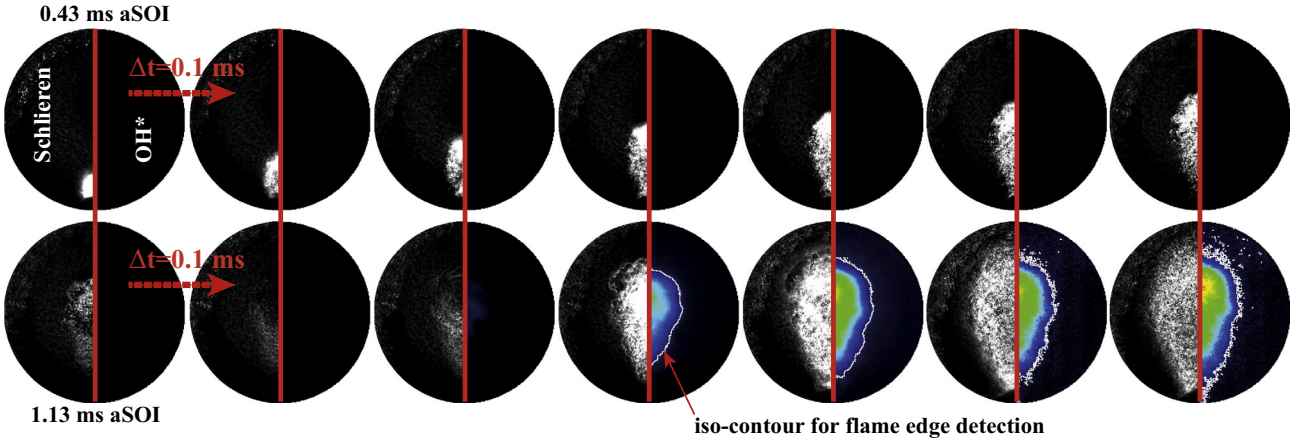

Fig. 13. Time series of schlieren (left half) and OH* chemiluminescence images (right half) for OP2 $\Phi_{CH_4} = 0.44$, starting $t = 0.43$ ms after hydraulic SOI of the pilot spray and an increment of $\Delta t = 0.1$ ms.

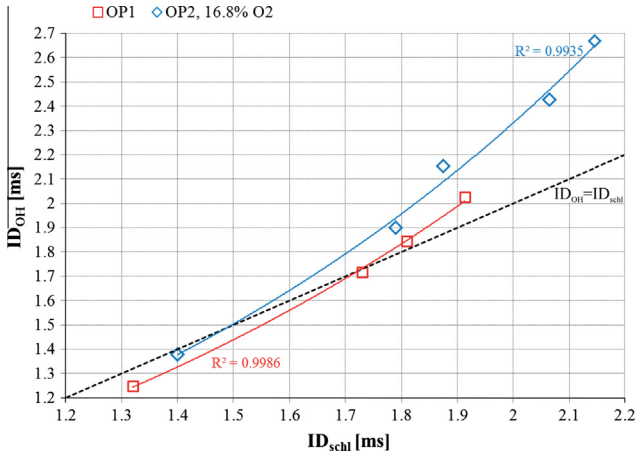

Fig. 14. Regression plot of ignition delays calculated by schlieren ID_{schl} and OH* PMT data ID_{OH}, solid lines represent exponential trendlines for better visibility.

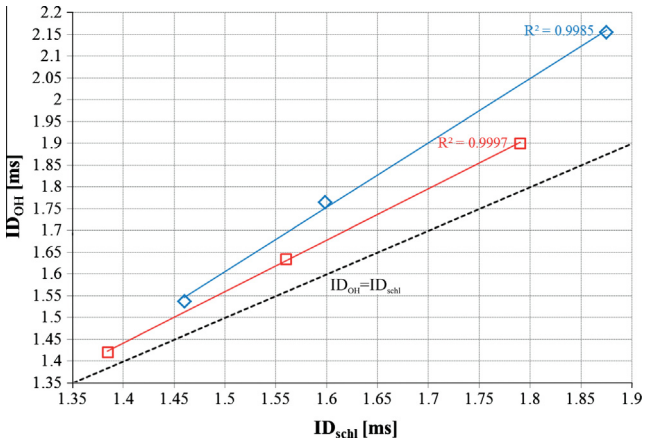

Fig. 16. Regression plot of ignition delays calculated by schlieren and OH* PMT data for a sweep in O_2 concentration and two constant methane masses with linear trendlines (solid), OP2.

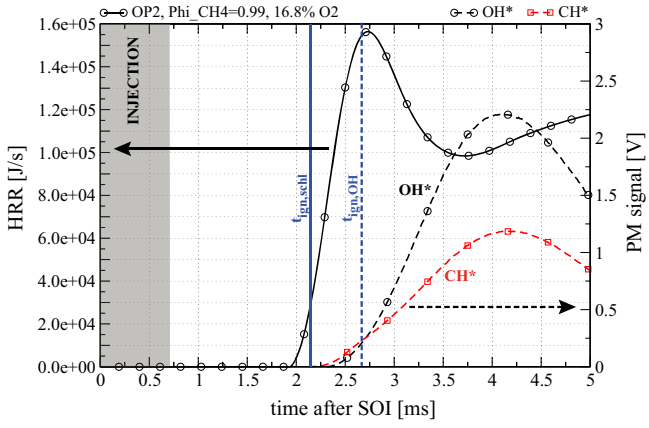

Fig. 15. Heat release rate, OH* and CH* PMT signals, dashed vertical line represents ID_{schl} and solid line ID^*_{OH}.

experiments before [38–40] and can be attributed to the CO–O emission spectrum characteristic to HCCI combustion. OH* and CH* chemiluminescence emission is very sensitive to temperature, pressure and local strain rate [41–44]. Also, the spectral emission during combustion is changing over time and is highly dependent on the type of combustion, mixing state and fuel [45–47]. The expected spectra for premixed combustion ignited by pilot spray are expected to change over time due to the hybrid nature of this specific combustion type. The first phase can exhibit a spectrum similar to a stratified charge compression ignition (n-heptane in air), characterized by a distinct OH* and CH* peak or an HCCI type broad spectrum which exhibits emissions over a wide range of wavelengths (n-heptane autoignition with CH_4 premixed and/or ambient oxygen concentration reduction) which is dependent on the equivalence ratio at which ignition and combustion occurs. The first phase is then followed by a transition to a spectrum during premixed combustion with distinct peaks for OH*, CH* and C_2^* at the respective wavelengths. Measurements for different spectra can be found in [47] for homogeneously and partially premixed combustion with spark ignition and HCCI combustion, supporting the explanation of a temporal change in emission spectra for dual fuel combustion.

Fig. 17 shows the ignition delay as a function of the methane equivalence ratio determined by schlieren image analysis as described before for most investigated operating points. The general trend of increasing ignition delays with increasing amounts of methane has been observed before by various researchers [12,9,16,17,48], indicating an influence of methane on the ignition reactions. Generally, lower temperatures lead to longer ignition delays and a higher sensitivity with respect to the influence of

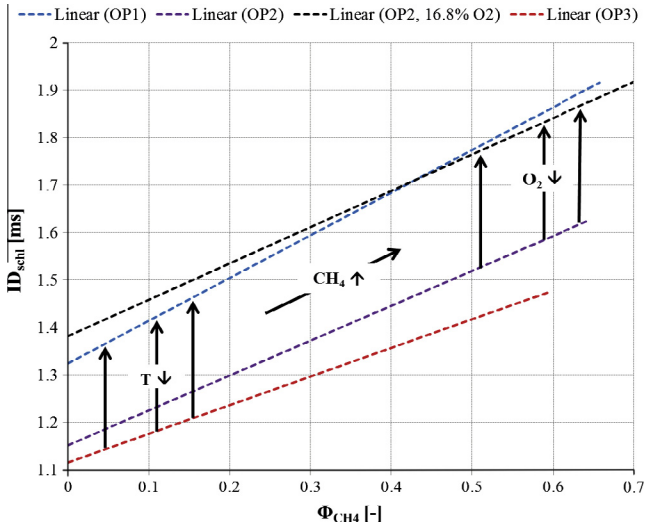

Fig. 17. Ignition delays based on schlieren image analysis as a function of methane equivalence ratio over a wide range of operating points.

methane since the slope of the linear trendlines is steeper for lower temperatures (OP1 vs. OP3). O_2 reduction causes an offset of the ignition delays while the chemical influence of the methane stays constant (OP2 vs OP2 16.8% O_2).

4.4.1. Ratio of CH* and OH* chemiluminescence

The used measurement equipment (PMT) is capable of detecting very low chemiluminescence emissions, allowing for the visualization of low temperature and high temperature ignition based on different wavelengths but the sensitivity of the system (the gain) is adjusted based on the maximum intensities detected in a range between 0 and 10 V over the whole combustion event. These maximum intensities are dependent on the area of the reaction zone and combustion mode which in the presented investigations usually lie somewhere in the early phases of premixed combustion, after the heat release due to the pilot spray ignition and combustion. The upper plot in Fig. 18 shows the heat release rate, the OH* photomultiplier signal and the calculated ignition delays based on schlieren images (solid blue vertical line) and OH* photomultiplier signal (dashed blue vertical line). In fact, the OH* PMT signal peaks after the initial heat release arising from the pilot spray, therefore leading to a prolonged ignition delay detection based on the OH* PMT signal. To increase the signal to noise ratio of the measured chemiluminescence intensity, the ratio of CH*/OH* can be plotted: not only is the timing of the second stage ignition apparent when the CH* intensity increases rapidly compared to the OH* emission, but also an earlier small increase in this ratio is detected (Fig. 18, lower), which can be attributed to the CH* emission during low temperature ignition, detectable due to the fact that the CH* chemiluminescence filter wavelength of 430 nm is well within the formaldehyde bands of characteristic spectra measured in HCCI combustion experiments [19]. After the second peak representing the high temperature ignition, higher OH* than CH* chemiluminescence emission is observed, where the ratio drops significantly.

However, due to the high sensitivity of the ratio to the absolute values of the PMT signal levels during low temperature ignition no post-processing of this low temperature ignition region was performed, which could be addressed with appropriate gain selection for photomultiplier measurements during the first stage ignition or the application of spectroscopic measurements for this phenomena in future investigations.

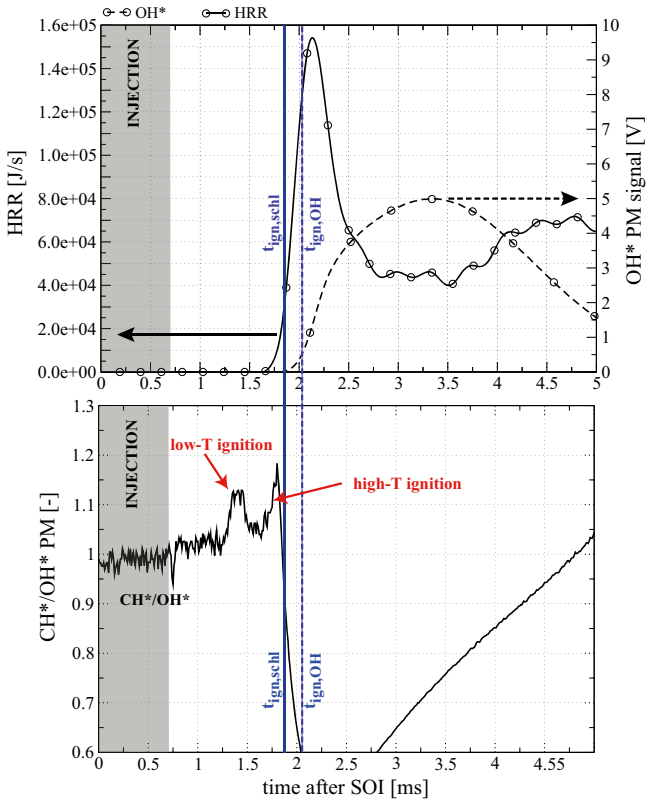

Fig. 18. Heat release rate and OH* PMT signal (upper), ratio of CH*/OH* PMT (lower) for OP1 $\Phi_{CH_4} = 0.66$. Blue vertical lines represent the high temperature ignition delay calculated with schlieren image (solid) and OH* photomultiplier (dashed) analysis. (For interpretation of the references to colour in this figure legend, the reader is referred to the web version of this article.)

4.5. Kinetic analysis of the chemical influence of methane on the pilot ignition delay

To support the interpretations given in the previous sections to the results and to gain insight into the chemical processes during the ignition phenomena of such a system, simulation tools capable of predicting the chemical reactions associated to combustion prove valuable. For this reason, simulations of an adiabatic constant pressure Perfectly Stirred Reactor (PSR, SENKIN) and a reaction mechanism for n-heptane with methane as a reactive component were carried out. The skeletal reaction mechanism employed consists of 44 species and 112 reactions and was originally developed to describe the behaviour of n-heptane autoignition [49]. A reduced variant thereof – also proposed in [49] – has been applied successfully in Direct Numerical Simulations of premixed methane flame initiation by n-heptane spray autoignition [30,50]. Another study to numerically investigate dual fuel combustion was recently published [37], applying an n-heptane kinetic mechanism with 40 species and 83 reactions from [51,52]. The researchers claim to have tested the reaction mechanism against GRI 3.0 for methane/air combustion in order to analyse its suitability for dual fuel combustion. However, only one reaction (not reversible) for the consumption of CH_4 in the slightly smaller reaction mechanism is present, e.g. $CH_4 + OH \Rightarrow H_2O + CH_3$. This reaction, governed by high temperature oxidation with OH, only represents one of the essential paths in which CH_4 can react to CH_3 under lean conditions highlighted by [53] and cannot trigger an ignition event when no OH is present, i.e. no autoignition can occur. Recent analysis of ignition in dual fuel mixture [54] has shown that this path is the main driver behind the chemical influence of methane on n-heptane autoignition

processes. In this study, the 44 species mechanism was used which contains 4 reversible reactions representing some of the essential paths in CH_4 oxidation.

In order to assess the mechanism's ability to account for the effect of methane a comparison of ignition delays for various methane/air mixtures computed with the above mechanism and GRI 3.0 [55] was performed over a wide range of temperatures and pressures for a constant equivalence ratio of $\Phi_{CH_4} = 0.5$, which represents approximately the most reactive mixture for methane autoignition [56]. The thermodynamic state of the constant pressure perfectly stirred reactor for the dual fuel investigations was chosen according to the average state of the cylinder content corresponding to the three experimentally investigated operating points (OP1–OP3) 0.5 ms after hydraulic start of injection for the pilot spray as shown in Table 4. The equivalence ratio of the pilot fuel n-heptane was held constant at $\Phi_{CH_7H_{16}} = 3.1$, corresponding to the most reactive mixture for n-heptane autoignition [30] at similar conditions.

Fig. 19 shows the calculated PSR ignition delays with the Liu mechanism in comparison to the GRI data and very good agreement over a wide range of temperatures and pressures for a fixed methane equivalence ratio $\Phi_{CH_4} = 0.5$ is achieved, even for low temperatures where ignition delays of the order of several seconds are calculated for both mechanisms.

Methane was added to the initial mixture in different amounts for a variation in methane equivalence ratio. The reaction mechanism was extended by an imaginary species $CH_{4,IM}$, which is inert but has the same thermal properties as CH_4. This extension allows for separation of the influence of CH_4, O_2 and n-heptane concentration by comparison of the reactivity for mixtures with various amounts of CH_4 and $CH_{4,IM}$, respectively. Fig. 20 shows the behaviour of two-stage autoignition characteristic to n-heptane. The black traces represent the reference case for each operating point, e.g. n-heptane in air, with neither CH_4 and $CH_{4,IM}$ present. With CH_4 or $CH_{4,IM}$ addition the ignition delays increase for all operating points. Also, the temperature rise during low temperature ignition decreases, but is seen to be mainly influenced by O_2 and n-heptane availability rather than reactions associated to methane. The decreasing O_2 concentration is responsible only for a part of the prolonged ignition delay, while the effect of reactive methane increases with increasing ambient methane content and decreasing temperatures, supporting the findings in [54]. In OP1, even small methane equivalence ratios double the effect of oxygen concentration on low and high temperature ignition, with reactive methane addition mainly influencing the low temperature ignition delay and keeping the interval between the ignition stages constant.

Table 4
PSR conditions chosen for the dual fuel ignition delay calculations.

Composition	OP1	OP2	OP3
	$\Phi_{C_7H_{16}} = 3.1$ $\Phi_{CH_4} = 0.0–0.8$		
T [K]	766	810	853
p [bar]		21.2	

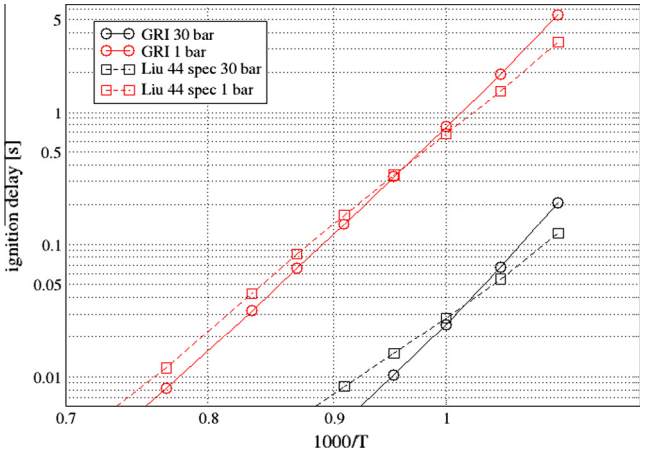

Fig. 19. Ignition delay calculations for homogeneous CH_4/air mixtures, comparison of Liu and GRI mechanism.

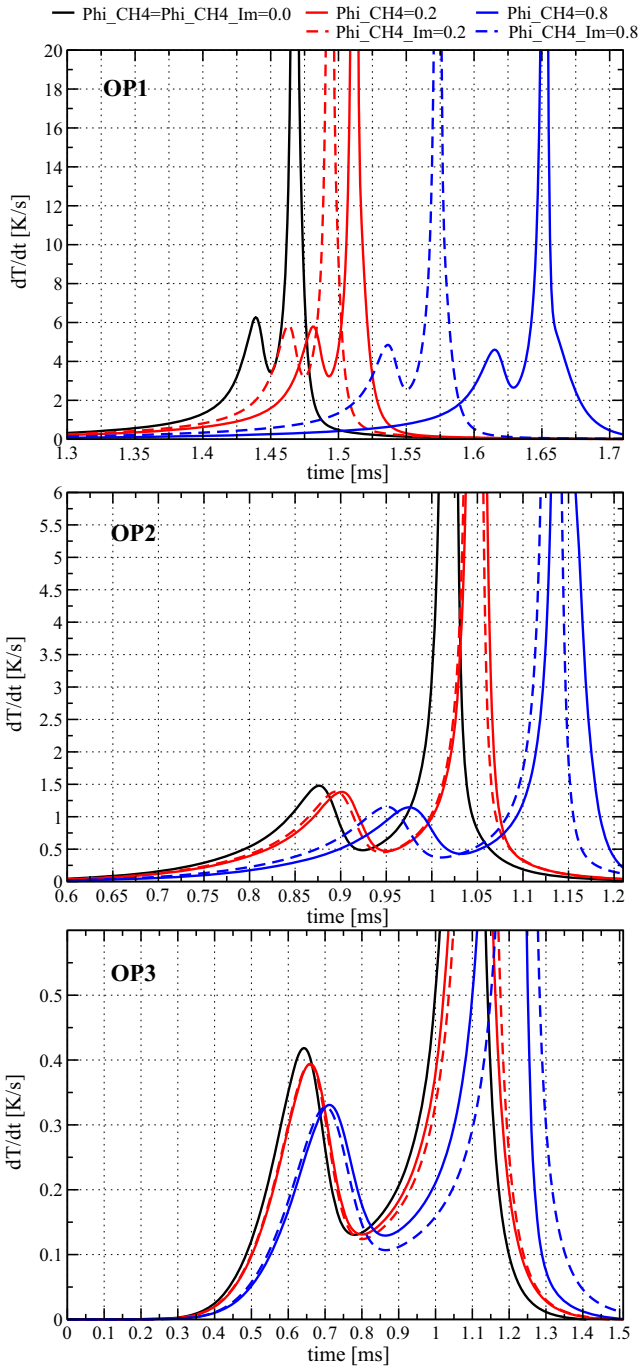

Fig. 20. Evolution of dT/dt for OP1 (top) during ignition, OP2 (middle) and OP3 (bottom). Comparison of two-stage ignition phenomena behaviour dependent on CH_4 (solid lines) and $CH_{4,IM}$ (dashed lines) equivalence ratio.

For higher temperatures, reactive methane addition prolongs first stage ignition reactions only marginally and primarily enhances the reactivity during the intermediate phase, while decreased oxygen availability tends to increase the time interval between the two ignition stages. In OP3, these effects lead to a reverse in high temperature ignition delay, most pronounced for $\Phi_{CH_4} = \Phi_{CH_4,IM} = 0.8$, where low temperature ignition with reactive methane addition happens later but high temperature ignition occurs earlier than the one with inert methane addition.

5. Summary and conclusions

The early phases of dual fuel combustion of homogeneous methane/air mixtures ignited by n-heptane micro pilots sprays were characterized experimentally in an optically accessible Rapid Compression Expansion Machine. A wide range of ambient equivalence ratios, three different temperatures, pilot fuel masses and ambient oxygen contents were examined at engine relevant conditions. A combination of high-speed OH* chemiluminescence and schlieren imaging was applied in conjunction with photomultiplier signals filtered at three different wavelengths in addition to thermodynamic analysis based on the pressure signal. Analysis of the pressure indication measurements and photomultiplier signals showed two distinct combustion phases, namely the ignition and combustion of the pilot spray and the subsequent premixed flame propagation in the lean methane/air mixture. Onset of high temperature ignition in the pilot spray region is influenced by the temperature of the surrounding mixture, methane content and oxygen availability (ambient O_2 concentration): increased ignition delays are observed for lower temperatures or higher dilutions leading to increased heat release rates during the pilot spray combustion phase as a consequence of higher entrainment of methane/air and improved mixing. Conversely, addition of methane prolongs the ignition delay and at the same time lowers the heat release during the pilot spray combustion phase. This was found to be due to inhibiting effects of the methane on the n-heptane ignition processes and the impact is more pronounced at colder conditions. These findings are supported by PSR calculations – allowing for separation of effects – using a reduced n-heptane oxidation scheme, capable of predicting two-stage ignition phenomena characteristic to n-heptane auto-ignition. Higher methane equivalence ratios, oxygen availability and temperature were seen to promote premixed flame propagation during the second combustion phase as expected and increased chemiluminescence emissions were observed, suggesting a dominant effect of the premixed combustion on the recorded OH* emissions. Flame area evolutions in the observable domain derived from 2D OH* chemiluminescence images confirm faster flame spread with increasing ambient methane equivalence ratios due to increased flame speeds. The analysis of the schlieren images allowed for determination of penetration lengths as well as the onset of high temperature ignition. Penetration lengths are found to increase at conditions with lower ambient density, while the timing of the disappearance of the spray schlieren signal decreases with increasing temperatures due to earlier low temperature ignition. Good agreement of the onset of high temperature ignition determined from OH* PMT signals, schlieren images and heat release rate analysis was found for operating points with low methane content. Due to the direct relationship between heat release and density-sensitive schlieren signal, the agreement in ignition delay persists for these two measurement methods. However, the onset of OH* chemiluminescence, i.e. determination of high temperature ignition, was seen to be delayed increasingly compared to heat release or schlieren analysis at higher methane equivalence ratios.

Acknowledgments

Financial support from the Swiss Federal Office of Energy (BfE, Grant No. SI/500644-01, SI/500818-01 and SI/500970-01) is gratefully acknowledged.

References

[1] Toulson E, Schock HJ, Attard WP. A review of pre-chamber initiated jet ignition combustion systems. Tech rep 2010-01-2236. SAE technical paper; 2010.
[2] Borges LH, Hollnagel C, Muraro W. Development of a Mercedes-Benz natural gas engine M 366 LAG, with a lean burn combustion system. Tech rep 962378. SAE technical paper; 1996.
[3] Cho HM, He B-Q. Spark ignition natural gas engines: a review. Energy Convers Manage 2007;48(2):608–18.
[4] Fukuzawa Y, Shimoda H, Kakuhama Y, Endo H, Tanaka K. Development of high efficiency miller cycle gas engine. Stroke 2001;2000:180.
[5] Ishida M, Tagai T, Ueki H. Effect of EGR and preheating on natural gas combustion assisted with gas-oil in a diesel engine. JSME Int J Ser B 2003;46 (1):124–30.
[6] Chen SK, Beck NJ. Gas engine combustion principles and applications. Tech rep 2001-01-0638. SAE technical paper; 2001.
[7] Karim GA. A review of combustion processes in the dual fuel engine: the gas diesel engine. Prog Energy Combust Sci 1980;6(3):277–85.
[8] Sahoo B, Sahoo N, Saha U. Effect of engine parameters and type of gaseous fuel on the performance of dual-fuel gas diesel engines–a critical review. Renew Sustain Energy Rev 2009;13(6):1151–84.
[9] Karim GA. Combustion in gas fueled compression: ignition engines of the dual fuel type. J Eng Gas Turbines Power 2003;125(3):827–36.
[10] Mbarawa M, Milton BE, Casey RT. Experiments and modelling of natural gas combustion ignited by a pilot diesel fuel spray. Int J Therm Sci 2001;40 (10):927–36.
[11] Choi I, Milton B. Dual-fuel combustion model for premixed natural gas with distillate ignition in a quiescent bomb. Numer Heat Transf Part A Appl 1997;31 (7):725–43.
[12] Iida N, Nakamura M, Ohashi H. Study of diesel spray combustion in an ambient gas containing hydrocarbon using a rapid compression machine. SAE Trans 1997;106(3):1537–45.
[13] Lee J-H, Iida N. Combustion of diesel spray injected into reacting atmosphere of propane-air homogeneous mixture. Int J Engine Res 2001;2(1):69–80.
[14] Saito H, Sakurai T, Sakonji T, Hirashima T, Kanno K. Study on lean burn gas engine using pilot oil as the ignition source. Tech rep 2001-01-0143. SAE technical paper; 2001.
[15] Carlucci AP, Laforgia D, Saracino R, Toto G. Study of combustion development in methane-diesel dual fuel engines. Based on the analysis of in-cylinder luminance. Tech rep 2010-01-1297. SAE technical paper; 2010.
[16] Schlatter S, Schneider B, Wright Y, Boulouchos K. Experimental study of ignition and combustion characteristics of a diesel pilot spray in a lean premixed methane/air charge using a rapid compression expansion machine. Tech rep 2012-01-0825. SAE technical paper; 2012.
[17] Schlatter S, Schneider B, Wright YM, Boulouchos K. Comparative study of ignition systems for lean burn gas engines in an optically accessible rapid compression expansion machine. Tech rep 2013-24-0112. SAE technical paper; 2013.
[18] Escher A, Kirchen P, Boulouchos K. Experimental investigations using a transparent single shot compression machine for HCCI-combustion. Tech rep 2007-24-0009. SAE technical paper; 2007.
[19] Mitakos D, Blomberg C, Vandersickel A, Wright Y, Schneider B, Boulouchos K. Ignition delays of different homogeneous fuel-air mixtures in a rapid compression expansion machine and comparison with a 3-stage-ignition model parameterized on shock tube data. SAE Int J Engines 2013;6 (4):1934–52.
[20] Barro C, Tschanz F, Obrecht P, Boulouchos K. Influence of post-injection parameters on soot formation and oxidation in a common-rail-diesel engine using multi-color-pyrometry. In: ASME 2012 internal combustion engine division fall technical conference. American Society of Mechanical Engineers; 2012. p. 293–302.
[21] Kirchen P, Obrecht P, Boulouchos K. Soot emission measurements and validation of a mean value soot model for common-rail diesel engines during transient operation. Tech rep 2009-01-1904. SAE technical paper; 2009.
[22] Kirchen P, Obrecht P, Boulouchos K, Bertola A. Exhaust-stream and in-cylinder measurements and analysis of the soot emissions from a common rail diesel engine using two fuels. J Eng Gas Turbines Power 2010;132(11):112804.
[23] Barro C, Obrecht P, Boulouchos K. Development and validation of a virtual soot sensor (VSS), Part 1: steady state engine operation. Int J Engine Res 2014;15 (6):719–30. http://dx.doi.org/10.1177/1468087413512309.
[24] Barro C, Obrecht P, Boulouchos K. Development and validation of a virtual soot sensor: Part 2: transient engine operation. Int J Engine Res 2015;16(2):127–36. http://dx.doi.org/10.1177/1468087414533786.
[25] Settles GS. Schlieren and shadowgraph techniques. Berlin: Springer-Verlag; 2001.
[26] Pickett LM, Kook S, Williams TC. Visualization of diesel spray penetration, cool-flame, ignition, high-temperature combustion, and soot formation using high-speed imaging. Tech rep 2009-01-0658. SAE technical paper; 2009.

[27] Skeen SA, Manin J, Pickett LM. Simultaneous formaldehyde PLIF and high-speed schlieren imaging for ignition visualization in high-pressure spray flames. Proc Combust Inst 2015;35(3):3167–74.
[28] Bobba M, Genzale C, Musculus M. Effect of ignition delay on in-cylinder soot characteristics of a heavy duty diesel engine operating at low temperature conditions. SAE Int J Engines 2009;2(1):911–24. http://dx.doi.org/10.4271/2009-01-0946.
[29] Farrace D, Bolla M, Wright YM, Boulouchos K. Predicting in-cylinder soot in a heavy-duty diesel engine for variations in SOI and TDC temperature using the conditional moment closure model. SAE Int J Engines 2013;6:1580–93.
[30] Demosthenous E, Borghesi G, Mastorakos E, Cant RS. Direct numerical simulations of premixed methane flame initiation by pilot n-heptane spray autoignition. Combust Flame 2016;163:122–37. http://dx.doi.org/10.1016/j.combustflame.2015.09.013.
[31] Huestis E, Erickson P, Musculus M. In-cylinder and exhaust soot in low-temperature combustion using a wide-range of EGR in a heavy-duty diesel engine. SAE technical paper 2007-01-4017. http://dx.doi.org/10.4271/2007-01-4017.
[32] Farrace D, Bolla M, Wright YM, Boulouchos K. Numerical study of the influence of EGR on in-cylinder soot characteristics in a heavy-duty diesel engine using CMC. SAE Int J Engines 2014;7:256–68.
[33] Benajes J, Payri R, Bardi M, Martí-Aldaraví P. Experimental characterization of diesel ignition and lift-off length using a single-hole ECN injector. Appl Therm Eng 2013;58(1):554–63.
[34] Kook S, Pickett LM. Liquid length and vapor penetration of conventional, Fischer–Tropsch, coal-derived, and surrogate fuel sprays at high-temperature and high-pressure ambient conditions. Fuel 2012;93:539–48.
[35] Pastor JV, Payri R, Garcia-Oliver JM, Briceño FJ. Schlieren methodology for the analysis of transient diesel flame evolution. Tech rep 2013-24-0041. SAE technical paper; 2013.
[36] Lillo PM, Pickett LM, Persson H, Andersson O, Kook S. Diesel spray ignition detection and spatial/temporal correction. Tech rep 2012-01-1239. SAE technical paper; 2012.
[37] Wang Z, Abraham J. Fundamental physics of flame development in an autoigniting dual fuel mixture. Proc Combust Inst 2015;35(1):1041–8.
[38] Anders H, Christensen M, Johansson B, Franke A, Richter M, Aldén M. A study of the homogeneous charge compression ignition combustion process by chemiluminescence imaging. Tech rep 1999-01-3680. SAE technical paper; 1999.
[39] Kumano K, Iida N. Analysis of the effect of charge inhomogeneity on HCCI combustion by chemiluminescence measurement. Tech rep 2004-01-1902. SAE technical paper; 2004.
[40] Dubreuil A, Foucher F, Mounaïm-Rousselle C. Analysis of flame and OH* natural emissions of n-Heptane combustion in a homogeneous charge compression ignition (HCCI) engine: effect of burnt gas dilution. Energy Fuels 2009;23(3):1406–11.
[41] Hardalupas Y, Orain M. Local measurements of the time-dependent heat release rate and equivalence ratio using chemiluminescent emission from a flame. Combust Flame 2004;139(3):188–207.
[42] Panoutsos C, Hardalupas Y, Taylor A. Numerical evaluation of equivalence ratio measurement using OH* and CH* chemiluminescence in premixed and non-premixed methane–air flames. Combust Flame 2009;156(2):273–91.
[43] Higgins B, McQuay M, Lacas F, Rolon J-C, Darabiha N, Candel S. Systematic measurements of OH chemiluminescence for fuel-lean, high-pressure, premixed, laminar flames. Fuel 2001;80(1):67–74.
[44] Higgins B, McQuay M, Lacas F, Candel S. An experimental study on the effect of pressure and strain rate on CH chemiluminescence of premixed fuel-lean methane/air flames. Fuel 2001;80(11):1583–91.
[45] Hwang W, Dec J, Sjöberg M. Spectroscopic and chemical-kinetic analysis of the phases of HCCI autoignition and combustion for single-and two-stage ignition fuels. Combust Flame 2008;154(3):387–409.
[46] Iijima A, Yoshida K, Shoji H. Optical measurement of autoignition and combustion behavior in an HCCI engine. Tech rep. SAE technical paper; 2010.
[47] Kim B, Kaneko M, Ikeda Y, Nakajima T. Detailed spectral analysis of the process of HCCI combustion. Proc Combust Inst 2002;29(1):671–7.
[48] Khalil E, Karim G. A kinetic investigation of the role of changes in the composition of natural gas in engine applications. J Eng Gas Turbines Power 2002;124(2):404–11.
[49] Liu S, Hewson JC, Chen JH, Pitsch H. Effects of strain rate on high-pressure nonpremixed n-heptane autoignition in counterflow. Combust Flame 2004;137(3):320–39.
[50] Demosthenous E, Borghesi G, Mastorakos E, Cant R. Direct numerical simulations of n-Heptane spray autoignition in methane-air mixtures relevant to dual-fuel engines. In: 52nd aerospace sciences meeting. American Institute of Aeronautics and Astronautics; 2014.
[51] Peters N, Paczko G, Seiser R, Seshadri K. Temperature cross-over and non-thermal runaway at two-stage ignition of N-Heptane. Combust Flame 2002;128(1):38–59.
[52] Yoshikawa T, Reitz RD. Development of an improved NO_x reaction mechanism for low temperature diesel combustion modeling. Tech rep 2008-01-2413. SAE technical paper; 2008.
[53] Frouzakis CE, Boulouchos K. Analysis and reduction of the CH_4-air mechanism at lean conditions. Combust Sci Technol 2000;159(1):281–303.
[54] Fu X, Aggarwal SK. Two-stage ignition and NTC phenomenon in diesel engines. Fuel 2015;144:188–96.
[55] Smith GP, Golden DM, Frenklach M, Moriarty NW, Eiteneer B, Goldenberg M, et al. GRI-MECH version 3.0. <http://www.me.berkeley.edu/gri_mech/>.
[56] Kim SH, Huh KY, Fraser RA. Modeling autoignition of a turbulent methane jet by the conditional moment closure model. Proc Combust Inst 2000;28(1):185–91.